Fluorescence molecular tomography system for *in vivo* tumor imaging in small animals

Jianwei Fu (傅建伟), Xiaoquan Yang (杨孝全), Guotao Quan (全国涛), and Hui Gong (龚 辉)*

Britton Chance Center for Biomedical Photonics, Wuhan National Laboratory for Optoelectronics, Huazhong University of Science and Technology, Wuhan 430074, China

**E-mail: huigong@mail.hust.edu.cn*

Received March 16, 2010

A fluorescence molecular tomography system for *in vivo* tumor imaging is developed using a 748-nm continuous wave diode laser as an excitation source. A high sensitivity cooled charge-coupled device (CCD) camera with excitation and emission filters is utilized to obtain the excitation and fluorescence images. The laser beam performs fast raster scanning using a dual-axis galvanometric scanner. The accuracy of the laser spot position at the source window is within ±200 μm. Based on the phantom experimental results, the spatial resolution is less than 1.7 mm, and the relative quantitation error is about 10%. *In vivo* imaging of a tumor-bearing nude mouse tagged with near-infrared dye demonstrates the feasibility of the system.

OCIS codes: 170.6960, 170.6280, 170.0110.

doi: 10.3788/COL20100811.1075.

Nanocarriers serve as carriers that can visualize incipient tumors *in vivo* in a non-invasive manner; these are also used to transport large quantities of drug molecules into cytosolic compartments of cells, helping achieve great progress in drug development[1−3]. In this field of study, it is essential to identify accurately the biodistribution of nanocarriers *in vivo* after administration to animals. Various imaging technologies, such as magnetic resonance imaging (MRI), positron emission tomography (PET), X-ray computed tomography (CT), and ultrasound, are widely used in this field[4−7]. However, MRI applications in molecular imaging are limited by its low sensitivity[8]. The main disadvantages of PET are the involvement of ionizing radiation and non-specific background[9]. Of the abovementioned technologies, CT and ultrasound are the most commonly used high-resolution anatomical imaging techniques; however, they are unable to provide molecular and functional information[10].

Optical imaging is important in conducting molecular imaging, especially when combined with specific fluorescent probes; over the years, it has become an emerging trend in the fundamental research and application areas[11,12]. Fluorescence molecular tomography (FMT) aims to obtain realistic three-dimensional (3D) imaging and quantification of fluorophore biodistribution in deep tissue. Multiple points on the tissue surface are illuminated successively, resulting in the identification of diffuse fluorescence originating from specific fluorescent probes. Spatially dependent fluorophore biodistribution can be obtained when FMT system is combined with a proper mathematical model describing light propagation in tissue. FMT has the ability to perform tumor growth and brain disease imaging; in addition, it can be used for chemotherapeutic treatment study and multispectral imaging[8,13−16].

A biomimetic nanocarrier has been developed in previous work, and its ability to directly transport functional cargo into the cytosol of cancer cells has been confirmed through a type of near-infrared dye[17]. In this letter, we present a slab geometry FMT system, which is tailored to 3D imaging of tumor tagged with this new nanocarrier. The laser spot positioning accuracy, spatial resolution, and quantitation accuracy are also evaluated. *In vivo* imaging of a tumor-bearing nude mouse is also performed.

A schematic of the FMT system is shown in Fig. 1. A 748-nm continuous wave (CW) diode laser (B&W TEK, Newark, Delaware) was used as the excitation source. The output laser beam was collimated, expanded, and then directed into the entrance of a dual-axis galvanometric scanner (Galvo Scanner ST8061, Shiji Tuotian, Beijing). A custom-made 160-mm f–θ lens coated with a 748-nm antireflection film was used to focus the laser beam on the source window. The diameter of the laser spot at the source window was about 400 μm. The typical laser power delivered to the source window was approximately 10 mW. The laser spot was directed on to the source window by rotating the mirrors with changeable input voltages. The voltages were provided by a data acquisition card (Anmai Zecheng, Beijing), which converted digital codes to analog voltages. The switching time between the adjacent points was 0.7 ms.

The imaging objects were fixed in the imaging chamber filled with optical property matching fluid. The chamber was made of transparent plastic with high optical transparency and low X-ray absorption. The thickness of the chamber walls was 2 mm. The optical properties of the matching fluid were approximately within the range of

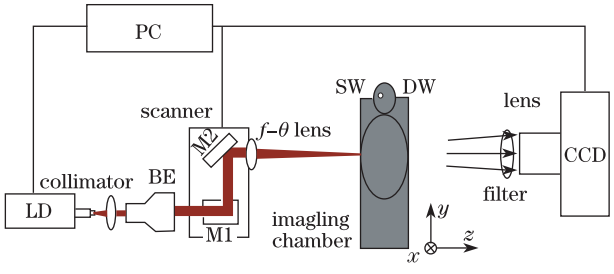

Fig. 1. FMT system. M1, M2: mirrors; BE: beam expander; DW: detection window; LD: laser diode; PC: personal computer; SW: source window

typical values of mammalian tissues[18,19]. The excitation laser went through tissues and excited the fluorophore to emit fluorescence. A high sensitivity cooled charge-coupled device (CCD) camera (ALTA U260, Apogee, RoseVille, California) with the resolution of 512×512 (pixel) was positioned on the opposite side of the laser. The maximum cooling temperature of the CCD chip was 50°C below ambient temperature. A 35-mm lens (Myutron, Tokyo) projected the imaging objects into the CCD. A band pass filter (750FS10-25, Andover Corp., Salem, New Hampshire) and a long pass filter (HQ770LP, Chroma, Bellows Falls) were placed in front of the CCD camera to capture the excitation and fluorescence light, respectively. The typical acquisition times for excitation and emission images were 0.03 and 1 s, respectively.

The scanning scope and spacing between adjacent laser spot positions were both determined prior to the data acquisition process. The exposure time was also adjusted to avoid blooming. The excitation and fluorescence images were recorded for each laser spot position. The total acquisition time was about 10 min when 5 excitation and fluorescence images were captured at each of the 11×11 positions. To determine the position of the laser spot, a piece of lens tissue was placed on the source window. The images of the laser spot were then recorded for each position using 4OD (OD: optical density) attenuators (transmittance 1×10^{-4}) in front of CCD camera.

In the CW domain, the propagation of excitation and emission light in biological tissue can be modeled through the following coupled diffusion equations:

$$\nabla \cdot [D_{\rm x}(r)\nabla\Phi_{\rm x}(r)] - [(\mu_{\rm ax}(r) + \mu_{\rm af}(r)]\Phi_{\rm x}(r) = -S_{\rm x}(r), \quad (1)$$

$$\nabla \cdot [D_{\rm m}(r)\nabla\Phi_{\rm m}(r)] - \mu_{\rm am}(r)\Phi_{\rm m}(r) = -\eta\mu_{\rm af}(r)\Phi_{\rm x}(r), \quad (2)$$

where subscripts x and m represent the excitation and emission wavelengths, respectively; $\Phi(r)$ is the photon density; $S(r)$ is the excitation source term; $\mu_{\rm a}(r)$ is the absorption coefficient; $D(r)$ is the diffusion coefficient; and $\eta\mu_{\rm af}(r)$ is the fluorescence yield of fluorophore. The diffusion equations can be solved using the Robin boundary condition presented as

$$\Phi(r) + 2aD(r)\frac{\partial\Phi(r)}{\partial n} = 0, \quad (3)$$

where a is the boundary mismatch coefficient due to the internal reflection at the boundary, and n is the normal vector. Utilizing finite element discretizing, the diffuse equations can be expressed as

$$\Phi_{i,j} = A_f[\alpha(x)], \ x \in \Omega, \quad (4)$$

where $\Phi_{i,j}$ is the photon density at the jth detector due to ith source, and $\alpha(x)$ is the fluorescence yield. In the experiment, the 3D distribution of fluorescence yield was reconstructed using the algebraic reconstruction technique (ART)[20]. For all image reconstructions, 41×20 virtual detectors were assumed to have fields of view of over 40.5×20 (mm). The volume of interest was segmented into 0.5×0.5×0.5 (mm) voxels, and the maximum iteration number was fixed at 100. The iterative process was terminated if the difference between the calculated values and measurements was smaller than 10^{-6} or if the iteration number exceeded 100.

The f–θ lens was designed to produce an off-axis spot at a location proportional to the deflection angles. Therefore, the coordinates of the laser spot on the source window were proportional to the input voltages applied to the scanner. The coordinate of the laser spot was assumed to be (0, 0) when the laser beam was directed vertically into the source window. In this case, the input voltages on both scanner axes were zero. The coordinates of the laser spot can be described using

$$y = d\theta, \quad x = (\sqrt{d^2 + y^2} + e)\theta, \quad (5)$$

where d is the distance between the rotation axis of mirror M2 and origin (0, 0) on source window, e is the distance between the two mirrors, and θ_x and θ_y are the deflection angles of the two mirrors, respectively.

The aforementioned method was used to obtain the detected position of each laser spot. Figure 2 depicts the discrepancy between the calculated and detected positions. The positions of the 11×11 laser spots on the source window are shown in Fig. 2(a). The calculated and detected positions are indicated with crosses and circles, respectively. Figures 2(b) and (c) show the discrepancies in x and y directions, respectively. The maximum discrepancy is smaller than 200 μm. Consequently, the reconstructed images showed very minor differences when either the calculated or detected position was adopted. Therefore, the acquisition process of the spot position is unnecessary for each experiment. In addition, this process can be used to calibrate the scanner.

Glass tube pairs (wall thickness: 100 μm; inner diameter: 2 mm) with different distances (1, 1.5, and 2.5 mm) were fixed in an imaging chamber filled with matching fluid (absorption coefficient $\mu_{\rm a} = 0.01$ mm^{-1} and reduced scattering coefficient $\mu_{\rm s}' = 2.1$ mm^{-1}). The tubes were both filled with 1-μmol/L DiR-BOA and placed about 5 mm away from the detection window. In these experiments, 21×11 laser spot positions with 1-mm spacing were considered. Figure 3 shows the reconstructed slices and line profiles. Figures 3(a)–(c) are the reconstructed slices, in which the distances between the two tubes are 1, 1.5, and 2.5 mm, respectively. Figures 3(d)–(f) are the corresponding line profiles of normalized reconstructed values marked by white lines in Figs. 3(a)–(c). These experiments demonstrate that the system has the ability to resolve two fluorophores placed at the distance of 1.7 mm.

A set of experiments was conducted to evaluate the ability of the system to resolve fluorophores with different concentrations. Glass tubes (wall thickness: 200 μm; inner diameter: 2.5 mm) filled with different DiR-BOA concentrations (100, 200,$\cdots$, 1000 nmol/L) were fixed in the imaging chamber with matching fluid ($\mu_{\rm a} = 0.01$ mm^{-1}, $\mu_{\rm s}' = 1.0$ mm^{-1}). The tubes were about 8 mm away from the detection window. In these experiments, 21×11 laser spot positions with 1-mm spacing were considered. The relationship between the average reconstructed values and the concentration is shown in

Fig. 4. The circles are the average reconstructed values, and the line indicates the linear regression. The maximum relative error is less than 10%.

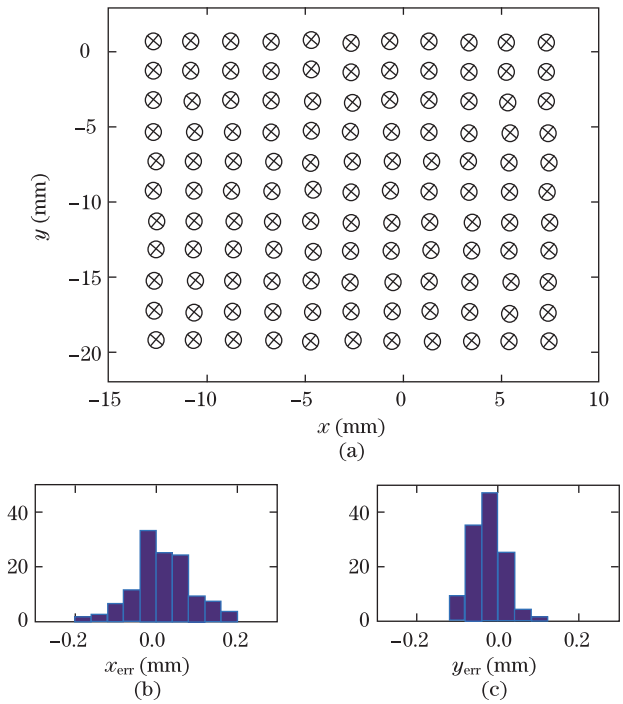

Fig. 2. Laser spot position accuracy. (a) Coordinates of the 11×11 laser spot positions (crosses represent the calculated positions and circles represent the detected positions); (b), (c) statistical discrepancies in x and y directions.

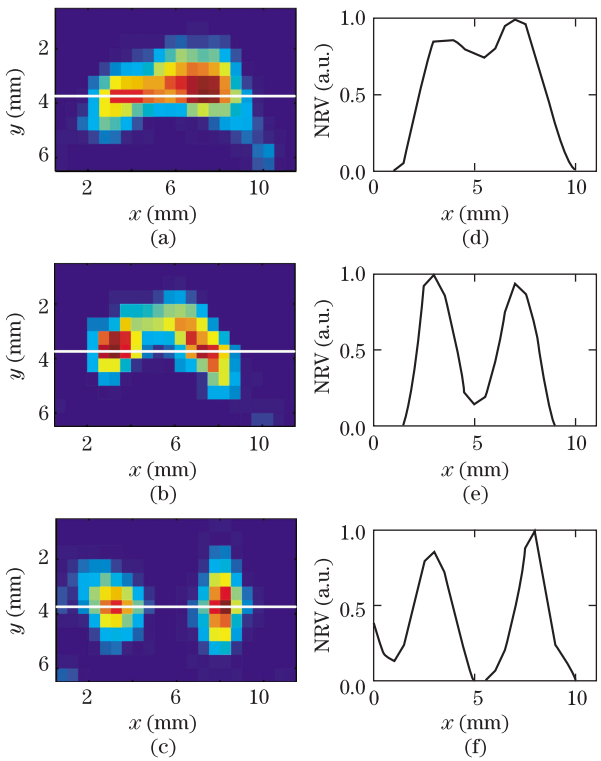

Fig. 3. Spatial resolution of the FMT system. (a)–(c) Constructed slices of tube pairs with distances of 1, 1.5, and 2.5 mm, respectively; (d)–(f) corresponding line profiles of normalized reconstructed values (denoted as NRV) indicated with white lines in (a)–(c).

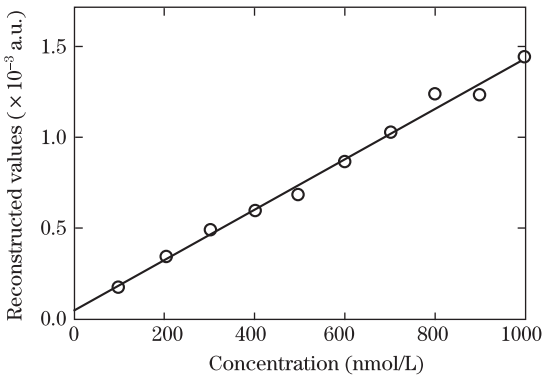

Fig. 4. Quantitation of the FMT system.

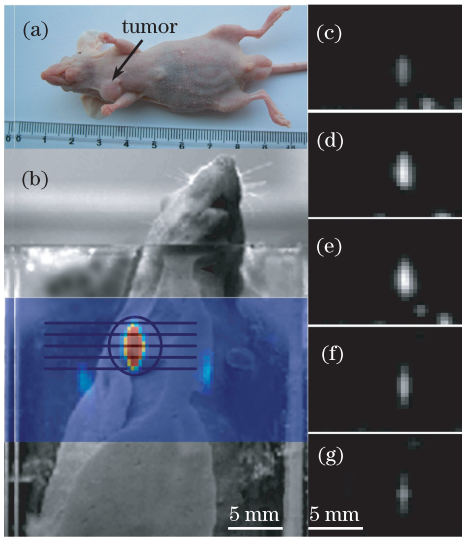

Fig. 5. Tumor imaging tagged with DiR-BOA. The tumor position is marked by a black arrow in (a); (b) the reconstructed pseudocolor fluorescence image is overlaid on the top of a grayscale photographic image of the nude mouse; (c)–(g) consecutive FMT slices obtained from top to bottom from the volume of interest shown on (b) by thin black horizontal lines.

To further test the feasibility of the system, ~2×10^6 nasopharyngeal carcinoma cells 5-8F were implanted into a 10-week-old female nude mouse weighing about 20 g. Four weeks after implantation, the size of tumor grew to about 7.1×6.4 (mm). Biomimetic nanocarriers correlated with a payload of DiR-BOA were transplanted intravenously. After two days, the nude mouse was anesthetized with a 9-mL/kg mixture of urethane (10%) and chloral hydrate (2%), and then fixed in the imaging chamber (40.5×13.5×60 (mm)). The tumor-bearing nude mouse tagged with DiR-BOA is shown in Fig. 5(a). The matching fluid ($\mu_a = 0.01$ mm^{-1} and $\mu_s' = 2.1$ mm^{-1}) was added, and the FMT acquisition and reconstruction processes were carried out. The reconstructed pseudocolor fluorescence image was overlaid on the top of a grayscale photographic image of the nude mouse (Fig. 5 (b)). The position and size of the tumor are shown by black circles, and the reconstructed area is colored blue. Figures 5(c)–(g) are the consecutive FMT slices as indicated by black lines from top to bottom in Fig. 5(b). The reconstructed images of the biodistribution of the nanocarriers reveal accurately the real tumor position. The ability of the

nanocarriers to transport functional cargo to tumor cells is thus confirmed.

In conclusion, a FMT system for small animal imaging is constructed and reported. The system is characterized by fast and accurate scanning of laser beam and high spatial sampling of the photon fields. The phantom experiments demonstrate the ability of the system to resolve two adjacent fluorophores and approximate the linear relationship between the reconstructed values and the concentration of the fluorescent dye. Furthermore, the *in vivo* experiment shows that the system can reveal the biodistribution of tumor-targeted biomimetic nanocarriers.

This work was supported by the National High-Tech Research and Development ("863") Program of China under Grant No. 2006AA020801.

References

1. M. Ferrari, Nat. Rev. Cancer **5,** 161 (2005).
2. D. Peer, J. M. Karp, S. Hong, O. C. Farokhzad, R. Margalit, and R. Langer, Nature Nanotechnol. **2,** 751 (2007).
3. R. Rezaeipoor, R. John, S. G. Adit, E. J. Chaney, M. Marjanovic, A. L. Oldenburg, S. A. Rinne, and S. A. Boppart, J. Innovative Opt. Health Sci. **2,** 387 (2009).
4. H. B. Na, I. C. Song, and T. Hyeon, Adv. Mater. **21,** 2133 (2009).
5. M. Nahrendorf, H. Zhang, S. Hembrador, P. Panizzi, D. E. Sosnovik, E. Aikawa, P. Libby, F. K. Swirski, and R. Weissleder, Circulation **117,** 379 (2008).
6. J. D. Woodward, S. J. Kennel, S. Mirzadeh, S. Dai, J. S. Wall, T. Richey, J. Avenell, and A. J. Rondinone, Nanotechnol. **18,** 175103 (2007).
7. S. H. Bloch, M. Wan, P. A. Dayton, and K. W. Ferrara, App. Phys. Lett. **84,** 631 (2004).
8. C. M. McCann, P. Waterman, J.-L. Figueiredo, E. Aikawa, R. Weissleder, and J. W. Chen, Neuroimage **45,** 360 (2009).
9. S. R. Cherry, Phys. Med. Biol. **49,** R13 (2004).
10. R. S. Balaban and V. A. Hampshire, ILAR J. **42,** 248 (2001).
11. V. Ntziachristos, J. Ripoll, L. V. Wang, and R. Weissleder, Nature Biotechnol. **23,** 313 (2005).
12. V. Ntziachristos, Annu. Rev. Biomed. Eng. **8,** 1 (2006).
13. S. V. Patwardhan, S. R. Bloch, S. Achilefu, and J. P. Culver, Opt. Express **13,** 2564 (2005).
14. A. Koenig, L. Hervé, V. Josserand, M. Berger, J. Boutet, A Da Silva, J.-M. Dinten, P. Peltié, J.-L. Coll, and P. Rizo, J. Biomed. Opt. **13,** 011008 (2008).
15. R. Bourayou, H. Boeth, H. Benav, T. Betz, U. Lindauer, T. Nierhaus, J. Klohs, A. Wunder, U. Dirnagl, and J. Steinbrink, J. Biomed. Opt. **13,** 041311 (2008).
16. M. Simantiraki, R. Favicchio, S. Psycharakis, G. Zacharakis, and J. Ripoll, J. Innovative Opt. Health Sci. **2,** 353 (2009).
17. Z. Zhang, W. Cao, H. Jin, J. F. Lovell, M. Yang, L. Ding, J. Chen, I. Corbin, Q. Luo, and G. Zheng, Angew. Chem. Int. Ed. **48,** 9171 (2009).
18. T. Troy, D. Jekic-McMullen, L. Sambucetti, and B. Rice, Mol. Imag. **3,** 9 (2004).
19. W.-F. Cheong, S. A. Prahl, and A. J. Welch, IEEE J. Quantum Electron. **26,** 2166 (1990).
20. A. C. Kak and M. Slaney, *Principles of Computerized Tomographic Imaging* (IEEE Press, New York, 2005).